



universe



Article

A Comprehensive Study on the Mid-Infrared Variability of Blazars

Xuemei Zhang, Zhipeng Hu, Weitian Huang and Lisheng Mao



<https://doi.org/10.3390/universe10090360>

Article

A Comprehensive Study on the Mid-Infrared Variability of Blazars

Xuemei Zhang ¹, Zhipeng Hu ², Weitian Huang ² and Lisheng Mao ^{2,*}¹ School of Mathematics, Yunnan Normal University, Kunming 650500, China; zhangxuemei@ynnu.edu.cn² Department of Physics, Yunnan Normal University, Kunming 650500, China; 2323090006@ynnu.edu.cn (Z.H.); huangweitian21@163.com (W.H.)

* Correspondence: maolisheng@ynnu.edu.cn

Abstract: We present a comprehensive investigation of mid-infrared (MIR) flux variability at $3.4\text{ }\mu\text{m}$ (W1 band) for a large sample of 3816 blazars, using Wide-field Infrared Survey Explorer (WISE) data through December 2022. The sample consists of 1740 flat-spectrum radio quasars (FSRQs), 1281 BL Lac objects (BL Lacs), and 795 blazars of uncertain type (BCUs). Considering Fermi Large Area Telescope detection, we classify 2331 as Fermi blazars and 1485 as non-Fermi blazars. Additionally, based on synchrotron peak frequency, the sample includes 2264 low-synchrotron peaked (LSP), 512 intermediate-synchrotron peaked (ISP), and 655 high-synchrotron peaked (HSP) sources. We conduct a comparative analysis of short- and long-term intrinsic variability amplitude (σ_m), duty cycle (DC), and ensemble structure function (ESF) across blazar subclasses. The median short-term σ_m values were $0.181_{-0.106}^{+0.153}$, $0.104_{-0.054}^{+0.101}$, $0.135_{-0.076}^{+0.154}$, $0.173_{-0.097}^{+0.158}$, $0.177_{-0.100}^{+0.156}$, $0.096_{-0.050}^{+0.109}$, and $0.106_{-0.058}^{+0.100}$ mag for FSRQs, BL Lacs, Fermi blazars, non-Fermi blazars, LSPs, ISPs, and HSPs, respectively. The median DC values were $71.03_{-22.48}^{+14.17}$, $64.02_{-22.86}^{+16.97}$, $68.96_{-25.52}^{+15.66}$, $69.40_{-22.17}^{+14.42}$, $71.24_{-21.36}^{+14.25}$, $63.03_{-33.19}^{+16.93}$, and $64.63_{-24.26}^{+15.88}$ percent for the same subclasses. The median long-term σ_m values were $0.137_{-0.105}^{+0.408}$, $0.171_{-0.132}^{+0.206}$, $0.282_{-0.184}^{+0.332}$, $0.071_{-0.062}^{+0.143}$, $0.218_{-0.174}^{+0.386}$, $0.173_{-0.132}^{+0.208}$, and $0.101_{-0.077}^{+0.161}$ mag for the same subclasses, respectively. Our results reveal significant differences in $3.4\text{ }\mu\text{m}$ flux variability among these subclasses. FSRQs (LSPs) exhibit larger σ_m and DC values compared to BL Lacs (ISPs and HSPs). Fermi blazars display higher long-term σ_m but lower short-term σ_m relative to non-Fermi blazars, while DC distributions between the two groups are similar. ESF analysis further confirms the greater variability of FSRQs, LSPs, and Fermi blazars across a wide range of time scales compared to BL Lacs, ISPs/HSPs, and non-Fermi blazars. These findings highlight a close correlation between MIR variability and blazar properties, providing valuable insights into the underlying physical mechanisms responsible for their emission.



Citation: Zhang, X.; Hu, Z.; Huang, W.; Mao, L. A Comprehensive Study on the Mid-Infrared Variability of Blazars. *Universe* **2024**, *10*, 360.

<https://doi.org/10.3390/universe10090360>

Academic Editor: Stephen J. Curran

Received: 27 July 2024

Revised: 27 August 2024

Accepted: 4 September 2024

Published: 7 September 2024



Copyright: © 2024 by the authors. Licensee MDPI, Basel, Switzerland. This article is an open access article distributed under the terms and conditions of the Creative Commons Attribution (CC BY) license (<https://creativecommons.org/licenses/by/4.0/>).

1. Introduction

Active galactic nuclei (AGNs), residing at the centers of most galaxies, are known to be powered by the accretion of matter onto their central supermassive black holes (SMBHs; 10^6 – 10^9 M_\odot) [1]. Approximately 10 percent of AGNs are classified as radio-loud, exhibiting powerful relativistic jets that often extend beyond the host galaxy [2,3]. A special subclass of radio-loud AGNs, blazars, are distinguished by their relativistic plasma jets oriented at small angles to our line of sight. This orientation significantly enhances their observed brightness through relativistic effects [3,4]. Blazars are characterized by rapid and dramatic flux variability across the electromagnetic spectrum, high polarization in the radio, optical, and X-ray bands, core-dominated radio structure, high luminosity, and strong γ -ray emission (e.g., [5–11]). Blazars can be further divided into BL Lacertae objects (BL Lacs) and Flat-Spectrum Radio Quasars (FSRQs) based on their

spectral properties. FSRQs show prominent emission lines in the optical band, while the spectra of BL Lacs are featureless or display weak lines only [12,13]. FSRQs are typically more luminous than BL Lacs [14–16]. The spectral energy distributions (SEDs) of blazars are characterized by two broad humps [17,18]. The low-energy hump is thought to be due to synchrotron emission from the relativistic electrons moving in a magnetic field inside the jet. The origin of the high-energy hump remains a topic of debate, with various leptonic and hadronic process models proposed [19]. Additionally, blazars can be classified based on the frequency of the synchrotron peak (ν_{peak}^s) as low-synchrotron peaked sources (LSPs; $\nu_{peak}^s \leq 10^{14}$ Hz), intermediate-synchrotron peaked sources (ISPs; 10^{14} Hz $< \nu_{peak}^s < 10^{15}$ Hz), or high-synchrotron peaked sources (HSPs; $\nu_{peak}^s \geq 10^{15}$ Hz) [20].

Blazars constitute the most numerous discrete extragalactic γ -ray sources identified in the Fermi Large Area Telescope (Fermi-LAT) sky maps [10]. The latest version (DR3) of the fourth Fermi-LAT AGN catalog (4LAC-DR3; [21]) incorporates 12 years of data, revealing 3407 high-latitude ($|b| > 10^\circ$) AGNs emitting high-energy γ -rays. These include 755 FSRQs, 1379 BL Lacs, 1208 blazars of uncertain type (BCUs), and 65 non-blazar AGNs. γ -ray loud blazars detected by Fermi-LAT are hereafter referred to as Fermi blazars. However, up to now, there are still thousands of known blazars that have not been detected to have significant γ -ray radiation during the Fermi-LAT's twelve years of continuous observations (e.g., [22–24]). Such γ -ray quiet blazars are hereafter referred to as non-Fermi blazars. Fermi blazars generally exhibit more extreme physical properties on average. These include higher jet power [25], larger radio Doppler factor [22,26], larger apparent opening angle and smaller viewing angle [27], faster apparent speeds [28,29], higher core flux density and brightness temperature [30], higher radio/optical polarization [7], and greater radio/optical variability [31,32].

Variability measurements serve as a powerful tool for unraveling the nature of AGNs and the dominant emission processes within them [33]. Blazars, as a population, are highly variable sources, but the underlying mechanisms remain a topic of debate. Variability in blazars has been detected in a wide range of time scales: intraday variability (IDV) with variations on time scales from minutes to hours or less than 1 day, short-term variability (STV) with variation on the order of days to months, and long-term variability (LTV) in time scales of months to several years or decades (e.g., [18,34–38]). Traditionally, blazar variability studies have focused on the radio, optical, X-ray, and γ -ray bands. In contrast, infrared variability has received less attention due to limited data and a smaller number of monitored sources (e.g., [36,39–41]), resulting in a gap in our understanding of this aspect. The advent of NASA's Wide-field Infrared Survey Explorer (WISE) presents a unique opportunity to study the variability properties of blazars from a statistical perspective [42–44].

Building upon previous studies [45,46], this work revisits the mid-infrared (MIR) variability properties of blazars. Using the WISE archival data from October 2013 to December 2017, we investigated the long-term MIR variability of a sample of 2573 blazars and compared variability amplitudes between FSRQs and BL Lacs, as well as Fermi and non-Fermi blazars [45]. Ref. [46] focused on a sample of 1035 Fermi blazars, systematically studying their MIR variability on both intraday and long time scales, with comparisons primarily between FSRQs and BL Lacs, as well as between LSPs, ISPs, and HSPs. This work addresses limitations present in both [45] and [46]. Our study utilizes a significantly larger blazar sample (3816 objects) compared to the previous works [45,46]. Additionally, we employ NEOWISE-R photometric data extending to December 2022, which surpasses the timespan used in [45,46]. Furthermore, the inclusion of AllWISE Multi-epoch Photometry data allows for extended light curves of selected sources. We comprehensively compare variability characteristics across various blazar subclasses: FSRQs vs. BL Lacs, Fermi vs. non-Fermi blazars, and LSPs vs. ISPs vs. HSPs. Our analysis encompasses both short- and long-term MIR variability. The ensemble structure function (ESF) method is employed to compare MIR variability amplitudes across different blazar populations on broad time scales.

The paper is organized as follows. Section 2 describes the sample and data used in the analysis. Section 3 presents the methods employed for characterizing temporal variability and the corresponding results. Finally, Section 4 provides a concise summary and discussion of the findings. It is important to note that all magnitudes reported throughout the paper are in the Vega system and uncorrected for Galactic extinction.

2. Sample and Data

The Wide-field Infrared Survey Explorer (WISE), a NASA Explorer mission, aimed to create the most comprehensive MIR sky survey ever undertaken. Launched in December 2009, WISE surveyed the entire sky in four MIR bands centered at 3.4 μm (W1), 4.6 μm (W2), 12 μm (W3), and 22 μm (W4) until its coolant depletion in September 2010 [42]. From October 2010 to February 2011, it continued observations in the W1 and W2 bands as part of the NEOWISE post-cryogenic mission before entering hibernation [43]. WISE photometric data obtained from 2010 to 2011 are publicly available in the AllWISE Multi-epoch Photometry data release¹. WISE was reactivated on 3 October 2013 and began sky scans solely in the W1 and W2 bands. This post-hibernation phase is known as the NEOWISE-R survey [44]². NEOWISE-R survey has scanned the sky nearly eighteen times in its first nine years, with six-month intervals between survey passes. During each observing epoch, 10–20 exposures are typically acquired over 1–2 days. Combining data from AllWISE and NEOWISE-R allows us to investigate both short-term and long-term MIR variability in AGNs.

Roma-BZCAT is the most comprehensive list of blazars compiled from multi-frequency surveys and literature reviews [47]. Its latest (fifth) edition incorporates data on 3561 blazars [10]. We cross-matched these blazars with those listed in the third and fourth catalogs of AGNs detected by Fermi-LAT [48,49]. This process yielded a combined sample of 4724 distinct blazars. To focus on high-latitude sources, we excluded objects located below an absolute galactic latitude ($|b|$) of 10 degrees. This resulted in a working sample of 4479 blazars. Sources identified in two Fermi-LAT catalogs (3LAC and 4LAC) were classified as Fermi blazars, while those exclusively listed in the Roma-BZCAT fifth edition (not present in Fermi-LAT catalogs) were designated as non-Fermi blazars.

We utilized the NASA/IPAC Infrared Science Archive (IRSA)³ to retrieve all photometric measurements at the W1 (3.4 μm) band for sources within a 5-arcsecond radius of the target coordinates. These data encompass all single-exposure detections from the WISE mission, including both the AllWISE and NEOWISE-R surveys, up to December 2022. Following established criteria from previous studies [46,50], we subsequently screened the retrieved AllWISE and NEOWISE-R data to exclude potentially unreliable photometric measurements⁴:

(1) Only detections (i.e., objects identified in the images) from framesets with $qual_fram > 0$ were retained. Framesets with $qual_frame = 0$ often indicate issues such as spurious detections of noise, transient events, or scattered light. By filtering out these framesets, we can ensure that the retained data are more likely to be reliable and representative of the targets being studied.

(2) qi_fact is the frame image quality score with a value of 1.0, 0.5, or 0.0, with 1.0 representing the best numerical image quality assigned to the single-exposure frameset and 0.0 the lowest. We selected database entries with $qi_fact = 1.0$, ensuring the best image quality.

(3) saa_sep is the angular separation between the apparent position of WISE and the boundary of the South Atlantic Anomaly (SAA). Positive saa_sep values indicate that WISE was outside of the SAA boundary, while negative saa_sep values indicate that WISE was within the SAA boundary. Framesets taken within the SAA exhibit elevated levels of charged particle hits that can induce spurious detections and contaminate measurements of real sources. We selected database entries with $saa_sep > 0$ to avoid framesets taken when the WISE spacecraft was within the boundaries of the SAA.

(4) The moon masking flag, *moon_masked*, indicates whether the frameset was taken within an area around the moon known to result in significant scattered light. We selected database entries where *moon_masked* = 0 to avoid detections that were made on frames potentially contaminated by scattered moonlight.

(5) The contamination and confusion flag, *cc_flags*, signifies whether the photometry and/or position measurements of a source were contaminated or biased due to proximity to an image artifact. Non-zero *cc_flags* values indicate that the single-exposure source database entry may be a spurious detection or that its measurements may be contaminated if it represents a real source. We selected detections that are not flagged as spurious detections or as real sources contaminated by image artifacts, i.e., those with *cc_flags* = 0.

(6) *nb* represents the number of point spread function (PSF) components simultaneously employed in the profile-fitting process for a source. This count includes the source itself, making the minimum value *nb* 1. When the source is fitted concurrently with other nearby detections (passive deblending), or when a single source is split into two components during the fitting procedure (active deblending), *nb* is greater than 1. To ensure accurate modeling, we retained only those detections that could be adequately represented using one or two PSF components, corresponding to *nb* \leq 2.

(7) The reduced chi-squared statistic, *w1rchi2*, quantifies the goodness-of-fit between the observed data at the W1 band (3.4 μ m) and the point spread function (PSF) model. By establishing a threshold of *w1rchi2* < 5, we exclude sources exhibiting a poor fit, thereby enhancing the overall quality and reliability of the retrieved photometric data.

(8) We only used measured magnitudes, that is, magnitudes for which an uncertainty is given, but no upper limits.

Finally, to facilitate the analysis of short- and long-term variability, we required a minimum of five photometric measurements per observing epoch and at least five epochs of data remaining for each source after filtering.

Our final sample comprises 3816 blazars, categorized as 1740 FSRQs, 1281 BL Lacs, and 795 BCUs. Figure 1 depicts the sky distribution of these blazars in Galactic coordinates. The positions of FSRQs, BL Lacs, and BCUs are marked with large red circles, medium blue crosses, and small cyan triangles, respectively. Redshift information is available for 2567 blazars (\sim 67%), detailed in Table 1 and Figure 2. Regarding Fermi-LAT detection, the sample includes 2331 Fermi blazars and 1485 non-Fermi blazars.

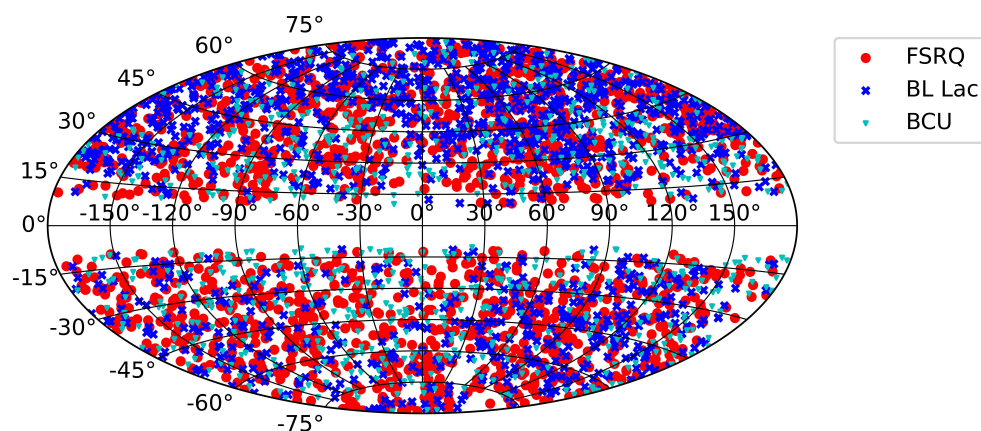


Figure 1. Sky distribution of selected blazars in Hammer-Aitoff projection with Galactic coordinates.

Table 1. Distribution of the number of blazar subclasses and their corresponding redshift (z) distributions.

Type	Number	Number-z *	z Range	Median z
FSRQ	1740	1740	0.07~6.802	1.2735
BL Lac	1281	622	0.000927~3.528223	0.3225
BCU	795	205	0.000927~4.413	0.66
Fermi blazar	2331	1215	0.000927~4.313	0.746
non-Fermi blazar	1485	1352	0.07~6.802	1.114
LSP	2264	1823	0.000927~5.47	1.196
ISP	512	271	0.000927~6.802	0.56
HSP	655	399	0.047~3.475	0.335

* Number of sources with available redshift data.

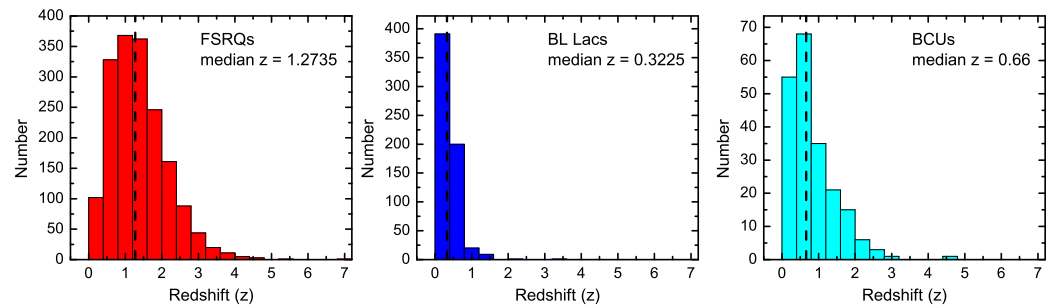


Figure 2. Redshift distributions of FSRQs, BL Lacs, and BCUs in the sample. The black dashed lines indicate the median redshifts of the three subsamples.

To classify these blazars, we used three spectral energy distribution (SED) peak frequency (ν_{peak}^s) categories: LSP ($\nu_{peak}^s \leq 10^{14}$ Hz), ISP (10^{14} Hz $< \nu_{peak}^s < 10^{15}$ Hz), and HSP ($\nu_{peak}^s \geq 10^{15}$ Hz) blazars. The peak frequencies were determined using data from Refs. [48,49,51] and the Open Universe for Blazars—Reference List V2.0 [52]⁵. Fermi blazars listed in the third catalog of AGNs detected by Fermi-LAT (3LAC) were initially classified based on their published ν_{peak}^s values ([48]; Table 4, Column 9). The remaining Fermi blazars were classified using ν_{peak}^s values from the fourth catalog of AGNs detected by Fermi-LAT (4LAC) ([49]; Table 3, *nu_syn* column). For Fermi blazars lacking ν_{peak}^s information in either catalog, and for all non-Fermi blazars, we first searched for potential ν_{peak}^s data in the Open Universe for Blazars—Reference List V2.0. Finally, for sources without ν_{peak}^s data in these references, we searched for potential ν_{peak}^s data in Ref. [51]. This process resulted in the classification of 2264 LSPs, 512 ISPs, and 655 HSPs.

We generated 69,503 short-term light curves for all sources, averaging approximately 18 light curves per source. A representative long-term light curve for a BL Lac (5BZB J1135+3200 at $z = 0.511$) is presented in Figure 3, along with one of its short-term light curves. Among the final sample of 3816 blazars, 3806 sources had 3.4 μ m photometric data available from both the AllWISE and NEOWISE-R surveys, spanning a 13-year period from MJD 55203 to MJD 59926. The remaining 10 sources had 3.4 μ m photometric data solely from the NEOWISE-R survey, covering a 9-year period from MJD 56655 to MJD 59926.

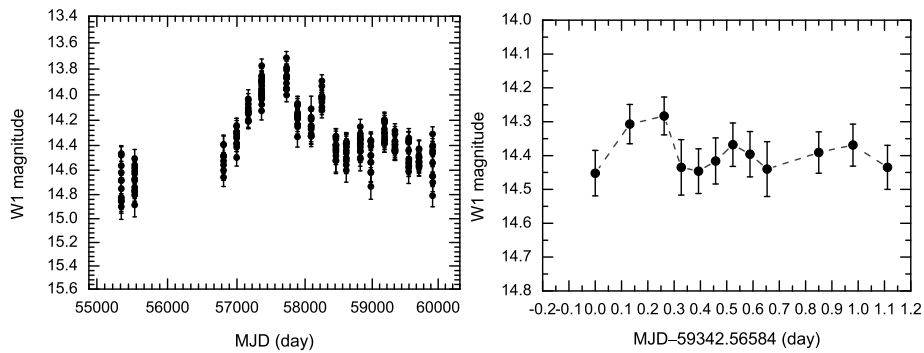


Figure 3. Light curves of the BL Lac 5BZB J1135+3200 ($z = 0.511$) in the W1 band: (Left) long-term light curve; (Right) representative short-term light curve.

3. Methods and Results

3.1. Short-Term Variability Amplitude

A crucial aspect of blazar research involves investigating the amplitude of variability observed in their light curves. One of the most widely used metrics for this purpose is the intrinsic amplitude of variability (σ_m) [53,54]. This parameter is derived by estimating the variance of the observed light curve after accounting for measurement errors. As described in Ref. [53], σ_m is calculated as follows:

$$\sigma_m = \begin{cases} \sqrt{\Sigma^2 - \epsilon^2} & \text{if } \Sigma > \epsilon, \\ 0 & \text{otherwise,} \end{cases} \quad (1)$$

where Σ is the standard deviation of the light curve defined as

$$\Sigma = \sqrt{\frac{1}{N-1} \sum_{i=1}^N (m_i - \bar{m})^2}, \quad (2)$$

where N is the number of observations, m_i is the i th magnitude, and \bar{m} is the weighted mean magnitude. The measurement uncertainty (ϵ^2) incorporates both individual measurement errors and systematic uncertainty:

$$\epsilon^2 = \frac{1}{N} \sum_{i=1}^N \epsilon_i^2 + \epsilon_s^2, \quad (3)$$

where ϵ_i represents the uncertainty associated with the i th magnitude and ϵ_s is the systematic uncertainty for the specific band. In the W1 band, the systematic uncertainty is 0.024 mag [55].

We computed the short-term variability amplitude (σ_m) for each of the 69,503 short-term light curves using Equation (1). For each individual source, we selected the maximum σ_m value for further analysis. Ref. [46] calculated median σ_m values for different blazar subclasses by aggregating all short-term light curves within each subclass. Their approach provides a measure of the typical short-term variability for a given subclass. In contrast, our method focuses on identifying the maximum σ_m value for each individual source across multiple short-term light curves, followed by a comparative analysis of these maximum values across blazar subclasses.

The rms-flux correlation, a statistical relationship between the root-mean-square amplitude of variability and the average flux, has been observed in some blazars [56–59], suggesting that the source is more variable when it is brighter. Consistent with this correlation, maximum σ_m values are likely indicative of high-state activity. During these periods, increased jet turbulence or accretion disk fluctuations may contribute to higher brightness and greater variability. Conversely, quiescent or low states are characterized by reduced emission and variability due to a relatively stable jet and accretion disk. By analyzing maximum σ_m values, we aim to explore the upper limits of variability and

complement the average variability analysis presented in [46]. A comparative analysis of both average and maximum σ_m distributions among various blazar subclasses offers a more nuanced understanding of the variability characteristics of blazars. For instance, one population of blazars might exhibit a similar distribution of average σ_m but a different distribution of maximum σ_m compared to another population of blazars.

The complete set of short-term σ_m values for all sources is provided in Table 2. Notably, only 23 blazars ($\sim 0.6\%$) out of the 3816 have a short-term σ_m of zero, indicating a high prevalence of short-term MIR variability in this blazar population. The entire sample exhibits a range of short-term σ_m values from 0 mag to 1.636 mag, with a median of 0.149 mag. The distribution of short-term σ_m for the entire sample is presented in the left panel of Figure 4.

Table 2. Classification and MIR variability analysis results of our blazar sample \ddagger .

No.	Name	RA (deg)	Dec (deg)	z	Type1	Type2 [†]	Type3	σ_m (long) (mag)	σ_m (short) (mag)	Duty Cycle (%)
1	5BZQJ0000–3221	0.0850	–32.3503	1.275	FSRQ	N	LSP	0.030	0.242	78.56
2	5BZQJ0001–1551	0.2721	–15.8519	2.044	FSRQ	N	LSP	0.024	0.267	100.00
3	5BZBJ0001–0746	0.3250	–7.7741		BL Lac	Y	ISP	0.593	0.036	
4	5BZBJ0001–0011	0.3395	–0.1944	0.462	BL Lac	Y	LSP	0.137	0.148	83.40
5	5BZBJ0002–0024	0.7382	–0.4131	0.523	BL Lac	N	LSP	0.143	0.103	70.65
6	5BZQJ0003+2129	0.8306	21.4957	0.45	FSRQ	N	LSP	0.091	0.043	27.98
7	5BZBJ0004–1148	1.0203	–11.8161		BL Lac	Y	LSP	0.265	0.071	
8	5BZQJ0004+4615	1.0674	46.2551	1.81	FSRQ	Y	LSP	0.780	0.397	92.55
9	5BZQJ0004–4736	1.1485	–47.6054	0.884	FSRQ	Y	LSP	0.390	0.219	81.17
10	5BZQJ0004+2019	1.1490	20.3285	0.677	FSRQ	N	LSP	0.657	0.280	79.04
11	5BZQJ0005–1648	1.3247	–16.8013	0.78	FSRQ	N	LSP	0.127	0.081	49.03
12	5BZQJ0005+0524	1.3342	5.4030	1.9	FSRQ	N	ISP	0.000	0.142	43.30
13	5BZQJ0005+3820	1.4883	38.3376	0.229	FSRQ	Y	LSP	0.134	0.037	29.48
14	5BZBJ0006–0623	1.5579	–6.3931	0.347	BL Lac	Y	LSP	0.894	0.058	31.05
15	5BZQJ0006–4245	1.5822	–42.7552	1.77	FSRQ	N	LSP	0.000	0.312	92.19
16	5BZQJ0006+2422	1.7033	24.3768	1.684	FSRQ	N	ISP	0.106	0.542	93.39
17	5BZQJ0007–6113	1.8358	–61.2184	0.857	FSRQ	N	LSP	0.179	0.418	90.71
18	5BZBJ0007+4712	1.9999	47.2021	0.28	BL Lac	Y	HSP	0.240	0.085	42.62
19	5BZQJ0008–2339	2.0015	–23.6550	1.412	FSRQ	N	LSP	0.000	0.097	54.51
20	5BZBJ0008–2339	2.1474	–23.6577	0.147	BL	Y	HSP	0.055	0.083	53.17

[†] In this column, “Y” and “N” denote Fermi and non-Fermi blazars, respectively. \ddagger The complete table is available online at the National Astronomical Data Center (NADC) of China: <https://paperdata.china-vo.org/MLS/2024/Universe/Table2.csv>, accessed on 24 July 2024.

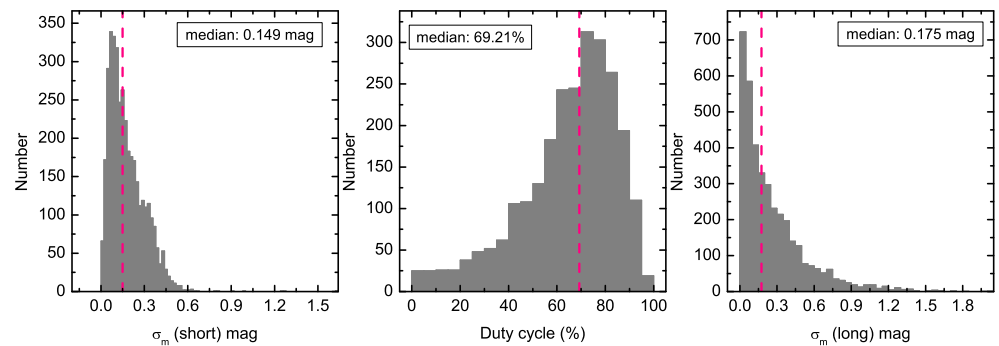


Figure 4. Distributions of (Left) short-term variability amplitude quantified by σ_m , (Middle) duty cycle, and (Right) long-term variability amplitude quantified by σ_m for the entire sample. The pink dashed lines mark the median values of the data set.

We investigated the short-term σ_m distributions for different blazar subclasses (FSRQs vs. BL Lacs, Fermi vs. non-Fermi blazars, and LSPs vs. ISPs vs. HSPs). Figure 5 illustrates the normalized histograms, cumulative distribution functions (CDFs), and quantile–quantile (Q–Q) plots for each subclass. To indicate the 95% confidence interval in the CDF plots, we used the 2.5th and 97.5th percentiles of 1000 bootstrapped CDFs derived from the original data. In the Q–Q plots, a 45-degree line is included to visually compare the distributions of the two samples. The same visualization approach is used in Figures 6 and 7.

To determine if the short-term σ_m distributions of FSRQs and BL Lacs differ significantly, we conducted a k -sample Anderson–Darling test using the `stats.anderson_ksamp` function within the SciPy scientific computing library [60,61]. The null hypothesis was that both distributions originate from the same source population. The k -sample Anderson–Darling test for FSRQs vs. BL Lacs resulted in a p -value $< 0.001^6$. The median short-term σ_m values were $0.181^{+0.153}_{-0.106}$ mag for FSRQs and $0.104^{+0.101}_{-0.054}$ mag for BL Lacs, respectively. A k -sample Kruskal–Wallis test, using the `stats.kruskal` function within the SciPy library, was employed to examine statistical differences between the medians of these groups [61,62]. The k -sample Kruskal–Wallis test yielded an H -statistic of 321.78 with a p -value of 5.93×10^{-72} . Based on the H -statistic, we calculated the effect size η^2 using the formula $\eta^2 = (H - k + 1) / (N - k)$, where k is the number of groups and N is the total sample size. General guidelines for interpreting effect sizes in this context are as follows: $\eta^2 < 0.01$ indicates a negligible effect, $0.01 \leq \eta^2 < 0.06$ a small effect, $0.06 \leq \eta^2 < 0.14$ a medium effect, and $\eta^2 \geq 0.14$ a large effect. The obtained η^2 was approximately 0.11, indicating a medium effect. The right-skewed distributions of short-term σ_m , as illustrated in Figure 5, necessitate an examination of the 75th and 95th percentiles to comprehend their shape and dispersion. For FSRQs, the 75th and 95th percentiles were 0.287 mag and 0.431 mag, respectively. For BL Lacs, these percentiles were 0.166 mag and 0.303 mag. These results collectively indicate statistically distinct short-term σ_m distributions between FSRQs and BL Lacs. Specifically, FSRQs exhibited significantly larger variability amplitudes on short time scales.

Figure 5 (middle panels, top to bottom) demonstrates a significant difference in the distributions of short-term σ_m between Fermi and non-Fermi blazars. A k -sample Anderson–Darling test resulted in a p -value less than 0.001, indicating statistically distinct distributions. The median short-term σ_m values were $0.135^{+0.154}_{-0.076}$ mag for Fermi blazars and $0.173^{+0.158}_{-0.097}$ mag for non-Fermi blazars, respectively. A k -sample Kruskal–Wallis test yielded an H -statistic of 78.83 with a p -value of 6.76×10^{-19} . The calculated effect size η^2 was approximately 0.02, indicating a small effect. The 75th and 95th percentiles of the short-term σ_m distribution for Fermi blazars were 0.226 mag and 0.390 mag, respectively. For non-Fermi blazars, these percentiles were 0.280 mag and 0.420 mag. These results indicate statistically distinct short-term σ_m distributions between Fermi and non-Fermi blazars, with non-Fermi blazars exhibiting larger variability amplitudes on short time scales.

We further examined the short-term σ_m distributions for LSPs, ISPs, and HSPs. The bottom panels of Figure 5 suggest that the short-term σ_m distribution of LSPs differs from those of ISPs and HSPs, while ISPs and HSPs appear to have similar distributions. A k -sample Anderson–Darling test resulted in a p -value less than 0.001, indicating statistically distinct distributions. The median short-term σ_m values were $0.177^{+0.156}_{-0.100}$ mag, $0.096^{+0.109}_{-0.050}$ mag, $0.106^{+0.100}_{-0.058}$ for LSPs, ISPs, and HSPs, respectively. A k -sample Kruskal–Wallis test yielded an H -statistic of 353.32 with a p -value of 1.89×10^{-77} . The calculated effect size η^2 was approximately 0.10, indicating a medium effect. We also calculated η^2 for pairwise Kruskal–Wallis tests. The results revealed a medium effect between LSPs and ISPs ($\eta^2 = 0.08$), a medium effect between LSPs and HSPs ($\eta^2 = 0.07$), and a negligible effect between ISPs and HSPs ($\eta^2 < 0.01$). To identify specific groups that differed significantly in their short-term σ_m distributions, we conducted Dunn’s test as a post-hoc analysis following the Kruskal–Wallis test. Dunn’s test determines whether the differences between the medians of various groups are statistically significant, adjusting for multiple comparisons [63]. We employed the “Bonferroni” method to adjust the p -values, using the `scikit-posthocs`

Python package for efficient implementation of Dunn's test⁷. The obtained adjusted p -values were 4.27×10^{-49} for the comparison between LSPs and ISPs, 2.99×10^{-46} for the comparison between LSPs and HSPs, and 0.41 for the comparison between ISPs and HSPs. In addition to comparing medians, we examined the 75th and 95th percentiles of the short-term σ_m distributions among LSPs, ISPs, and HSPs. For LSPs, the 75th and 95th percentiles were 0.284 mag and 0.427 mag, respectively. For ISPs, these percentiles were 0.157 mag and 0.298 mag. For HSPs, they were 0.170 mag and 0.300 mag. These results collectively suggest that LSPs exhibited significantly larger short-term σ_m compared to ISPs and HSPs, while ISPs and HSPs had comparable short-term σ_m values.

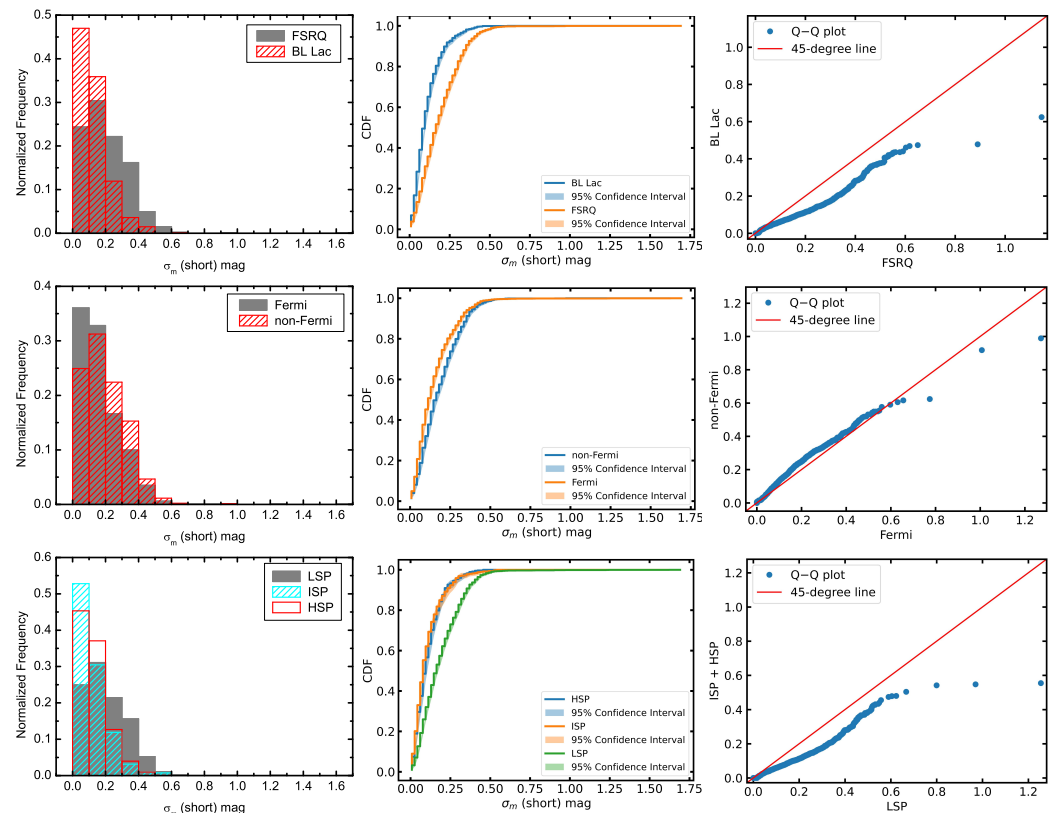


Figure 5. Distributions of short-term σ_m for different subclasses of blazars. (Left) panels show normalized histograms. (Middle) panels display CDFs with 95% confidence intervals. (Right) panels present Q–Q plots, with red lines representing 45-degree lines.

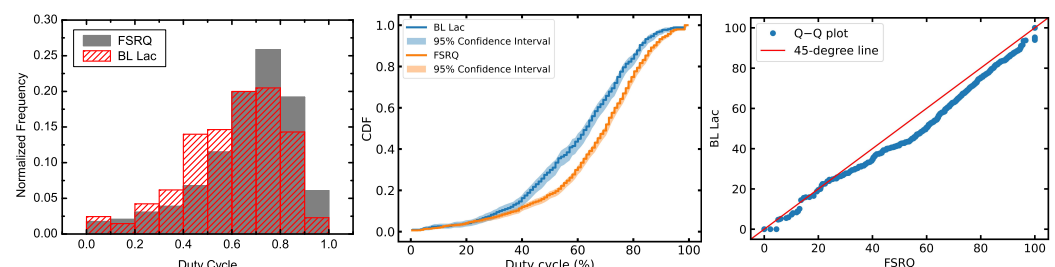


Figure 6. Cont.

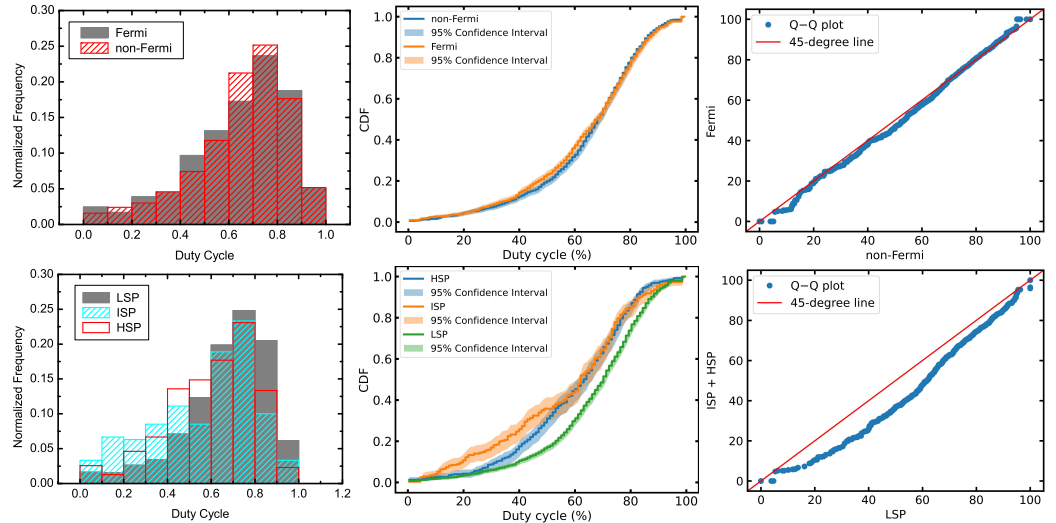


Figure 6. Distributions of duty cycle (DC) for different subclasses of blazars. Left panels show normalized histograms. Middle panels display CDFs with 95% confidence intervals. Right panels present Q–Q plots, with red lines representing 45-degree lines.

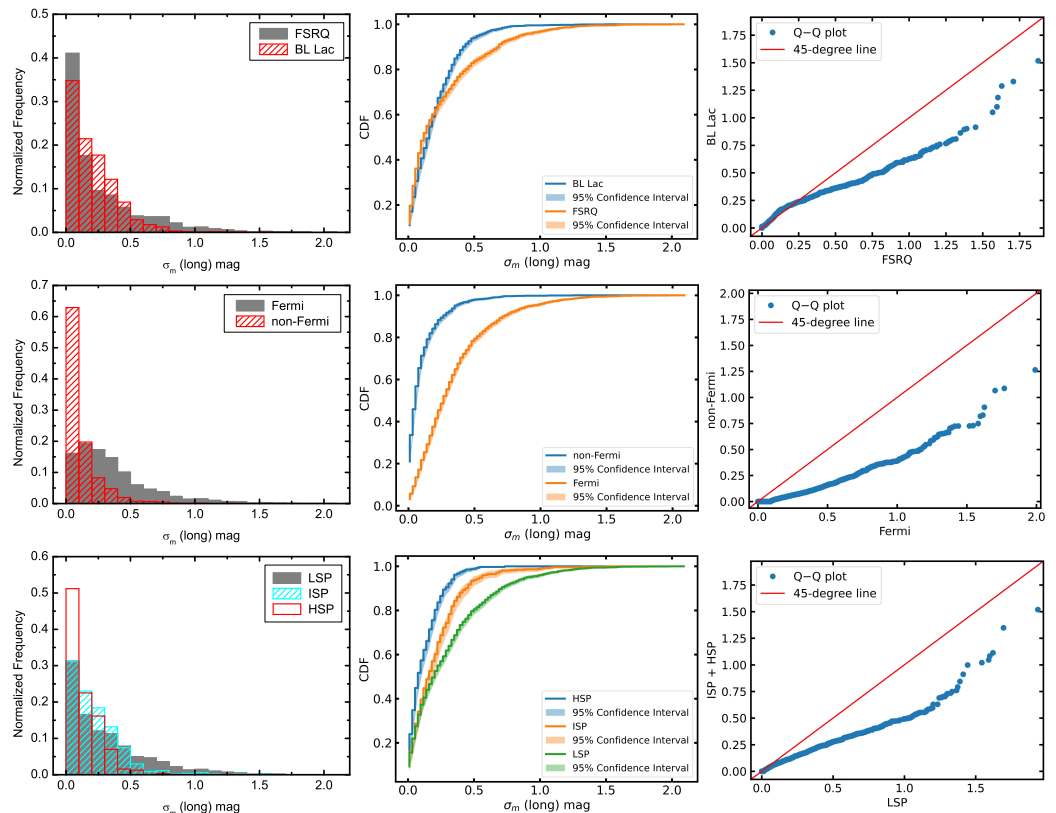


Figure 7. Distributions of long-term σ_m for different subclasses of blazars. (Left) panels show normalized histograms. (Middle) panels display CDFs with 95% confidence intervals. (Right) panels present Q–Q plots, with red lines representing 45-degree lines.

3.2. Duty Cycle

For each blazar in the sample, we obtained multiple short-term light curves, averaging approximately 18 per blazar. These light curves typically spanned $\sim 1\text{--}2$ days. We used these data to estimate the duty cycle (DC) of short-term variability, defined as the fraction of time a source exhibits an active phase (flux exceeding a given threshold) or variability relative to the total observation period. This metric accounts for the fact that blazars may

not display flux variations during all observational epochs. Following [64], the DC is calculated as

$$DC = \frac{\sum_{j=1}^M A_j \times (1/\Delta T_j)}{\sum_{j=1}^M (1/\Delta T_j)} \times 100\%, \quad (4)$$

where ΔT_j is the redshift-corrected time interval of the j th light curve ($\Delta T_j = \Delta T_{j,obs}(1+z)^{-1}$), M is the number of short-term light curves for a given source, and A_j is assigned a value of 1 for variable sources and 0 otherwise. Variability was determined using the criterion $\sigma_m > 0$ as outlined in Ref. [46]. We calculated the DC for 2567 blazars with known redshifts, as tabulated in Table 2. The overall DC distribution is shown in the middle panel of Figure 4. Only 19 blazars ($\sim 0.5\%$) exhibited a DC of 0. The median DC for the sample was approximately 69.21%. These findings collectively indicate that blazars, as a population of AGNs, display frequent short-term variability.

To compare the distributions of DC among various blazar subclasses, we analyzed the 2567 sources with computed DC values. A k -sample Anderson–Darling test between FSRQs and BL Lacs resulted in a p -value less than 0.001, indicating statistically distinct distributions (see Figure 6, upper panels). FSRQs and BL Lacs exhibited median DC values of $71.03^{+14.17\%}_{-22.48\%}$ and $64.02^{+16.97\%}_{-22.86\%}$, respectively. A k -sample Kruskal–Wallis test yielded an H -statistic of 51.63 with a p -value of 6.69×10^{-13} . The calculated effect size η^2 was approximately 0.02, suggesting a small effect. As illustrated in Figure 6, the distributions of DC values exhibit a pronounced left-skewness. To gain a more nuanced understanding of their shapes and dispersions, it is essential to analyze the 5th and 25th percentiles. For FSRQs, the 5th and 25th percentiles of the DC distributions were 23.97% and 57.70%, respectively. For BL Lacs, these percentiles were 24.60% and 48.00%. These results demonstrate that FSRQs exhibited larger DC values compared to BL Lacs.

Figure 6 (middle panels, top to bottom) indicates that the DC distributions of Fermi and non-Fermi blazars are not significantly different. This finding was supported by a k -sample Anderson–Darling test, which yielded a p -value of 0.16. The median DC values for Fermi and non-Fermi blazars were $68.96^{+15.66\%}_{-25.52\%}$ and $69.40^{+14.42\%}_{-22.17\%}$, respectively. A k -sample Kruskal–Wallis test resulted in an H -statistic of 0.63 with a p -value of 6.69×10^{-13} . The calculated effect size η^2 was less than 0.01, suggesting a negligible effect. For Fermi blazars, the 5th and 25th percentiles of the DC distributions were 23.26% and 53.53%, respectively. For non-Fermi blazars, these percentiles were 23.88% and 55.80%. These findings suggest that there were no statistically significant disparities in the distributions of DC values between Fermi and non-Fermi blazars, and that their DC values were comparable.

The bottom panels of Figure 6 illustrate the DC distributions for LSPs, ISPs, and HSPs. A k -sample Anderson–Darling test revealed a p -value less than 0.001, indicating statistically distinct distributions among these subclasses. The median DC values are $71.24^{+14.25\%}_{-21.36\%}$, $63.03^{+16.93\%}_{-33.19\%}$, and $64.63^{+15.88\%}_{-24.26\%}$ for LSPs, ISPs, and HSPs, respectively. A k -sample Kruskal–Wallis test yielded an H -statistic of 74.65 with a p -value of 6.16×10^{-17} . The calculated effect size η^2 was approximately 0.03, suggesting a small effect. We also calculated η^2 for pairwise Kruskal–Wallis tests. The results revealed a small effect between LSPs and ISPs ($\eta^2 = 0.02$), a small effect between LSPs and HSPs ($\eta^2 = 0.02$), and a negligible effect between ISPs and HSPs ($\eta^2 < 0.01$). Moreover, we conducted Dunn’s test as a post-hoc analysis following the Kruskal–Wallis test. The obtained adjusted p -values were 1.83×10^{-10} for the comparison between LSPs and ISPs, 1.45×10^{-10} for the comparison between LSPs and HSPs, and $\simeq 1.0$ for the comparison between ISPs and HSPs. In addition to comparing medians, we examined the 5th and 25th percentiles of the DC distributions among LSPs, ISPs, and HSPs. For LSPs, the 5th and 25th percentiles were 27.21% and 57.83%, respectively. For ISPs, these percentiles were 12.00% and 40.70%. For HSPs, they were 24.80% and 48.00%. These results jointly indicate that LSPs exhibited higher DC values compared to both ISPs and HSPs.

3.3. Long-Term Variability Amplitude

To investigate the long-term variability amplitude of selected blazars, we initially computed the mean MJD, W1 magnitude, and associated uncertainty for each observational epoch (typically spanning \sim 1–2 days). This process generated a representative long-term light curve for each blazar. The weighted average W1 magnitude, \bar{m}_{wtd} , is computed as

$$\bar{m}_{\text{wtd}} = \frac{\sum_{i=1}^N \omega_i m_i}{\sum_{i=1}^N \omega_i}, \quad (5)$$

where N is the number of photometric data points, m_i represents the i th magnitude, $\omega_i = 1/\sigma_i^2$ is the weight, and σ_i denotes the uncertainty of m_i . The standard error of the weighted average, as described in Ref. [65], is given by

$$\sigma_{\bar{m}_{\text{wtd}}} = \sqrt{\frac{1}{N-1} \left[\frac{\sum_{i=1}^N \omega_i m_i^2}{\sum_{i=1}^N \omega_i} - (\bar{m}_{\text{wtd}})^2 \right]}. \quad (6)$$

We subsequently applied Equation (1) to determine the long-term σ_m for all blazars. The resulting values are presented in Table 2, and the overall distribution of long-term σ_m is depicted in the right panel of Figure 4. The median long-term σ_m for the sample was found to be 0.175 mag.

When comparing the long-term σ_m distributions between FSRQs and BL Lacs, a k -sample Anderson–Darling test resulted in a p -value less than 0.001, indicating statistically distinct distributions (see Figure 7, upper panels). FSRQs and BL Lacs exhibited median long-term σ_m of $0.137^{+0.408}_{-0.105}$ and $0.171^{+0.206}_{-0.132}$, respectively. A k -sample Kruskal–Wallis test yielded an H -statistic of 0.06 with a p -value of 0.81. The calculated effect size η^2 was less than 0.01, suggesting a negligible effect. These results demonstrate that FSRQs and BL Lacs have different distributions of long-term σ_m , but their median values are similar. While their central tendencies are comparable, their overall shapes and spread vary. The normalized histograms reveal that FSRQs have a heavier tail. The CDFs plot shows a crossover between the two subclasses. The Q–Q plot further illustrates this difference: within the range of $\sigma_m < 0.25$ mag, the percentile points align with the 45-degree line, indicating similar distributions. However, within the range of $\sigma_m > 0.25$ mag, all points from FSRQs lie below the 45-degree line, suggesting that FSRQs tend to extend to larger σ_m values than BL Lacs. To quantify this difference, we computed the 75th and 95th percentiles of the long-term σ_m distributions for FSRQs and BL Lacs. The results were 0.383 mag and 0.306 mag for the 75th percentile, and 0.868 mag and 0.553 mag for the 95th percentile, respectively. If we adopt a more stringent criterion of 0.5 mag for long-term σ_m , 87 out of 1381 BL Lacs (\sim 6.8%) have a long-term σ_m value greater than 0.5 mag, while 305 out of 1740 FSRQs (\sim 17.5%) show a long-term σ_m larger than 0.5 mag. These findings collectively indicate that FSRQs tend to exhibit larger long-term σ_m values compared to BL Lacs.

Figure 7 (middle panels, top to bottom) presents a comparison of the long-term σ_m distributions for Fermi and non-Fermi blazars. A k -sample Anderson–Darling test revealed statistically significant differences between the two groups, with a p -value less than 0.001. Fermi blazars demonstrated a median long-term σ_m of $0.282^{+0.332}_{-0.184}$, significantly higher than that of non-Fermi blazars, which had a median of $0.071^{+0.143}_{-0.062}$. A k -sample Kruskal–Wallis test confirmed this disparity, yielding an H -statistic of 1083.58 with a p -value of 1.22×10^{-237} . The calculated effect size η^2 was 0.28, suggesting a large effect. The 75th and 95th percentiles of the long-term σ_m distribution for Fermi blazars were 0.476 mag and 0.958 mag, respectively. For non-Fermi blazars, these percentiles were 0.147 mag and

0.378 mag. These findings indicate that Fermi blazars exhibited significantly larger long-term σ_m values compared to non-Fermi blazars.

Figure 7 (bottom panels) presents a comparison of the long-term σ_m distributions for LSPs, ISPs, and HSPs. A k -sample Anderson–Darling test yielded a p -value less than 0.001, indicating statistically distinct distributions among these subclasses. The median long-term σ_m values were $0.218^{+0.386}_{-0.174}$, $0.173^{+0.208}_{-0.132}$, and $0.101^{+0.161}_{-0.077}$ for LSPs, ISPs, and HSPs, respectively. A k -sample Kruskal–Wallis test yielded an H -statistic of 180.45 with a p -value of 6.53×10^{-40} . The calculated effect size η^2 of approximately 0.05 indicates a small effect. We also calculated η^2 for pairwise Kruskal–Wallis tests. The results revealed a negligible effect between LSPs and ISPs ($\eta^2 < 0.01$), a medium effect between LSPs and HSPs ($\eta^2 = 0.06$), and a medium effect between ISPs and HSPs ($\eta^2 = 0.05$). A post-hoc Dunn’s test revealed significant differences between LSPs and ISPs (adjusted p -value = 9.54×10^{-5}), LSPs and HSPs (adjusted p -value = 3.45×10^{-40}), and ISPs and HSPs (adjusted p -value = 1.31×10^{-10}). In addition to comparing medians, we examined the 75th and 95th percentiles of the long-term σ_m distributions among LSPs, ISPs, and HSPs. For LSPs, the 75th and 95th percentiles were 0.447 mag and 0.927 mag, respectively. For ISPs, these percentiles were 0.321 mag and 0.573 mag. For HSPs, they were 0.209 mag and 0.374 mag. These findings suggest that LSPs exhibited larger long-term σ_m values compared to both ISPs and HSPs.

To complement our analysis of long-term variability using σ_m , we employed the structure function (SF) to investigate variability behavior across different time scales. As a powerful, model-independent tool for empirically quantifying AGN variability, the SF measures the root-mean-square variability of sources. Given the sparse sampling of WISE data, we calculated the ensemble structure function (ESF) to characterize the average variability of different blazar subclasses [66]. Following Refs. [46,67], the ESF is defined as

$$SF = \sqrt{\frac{\pi}{2} \langle |\Delta m|^2 \rangle - \langle \sigma_e^2 \rangle}, \quad (7)$$

where Δm is the magnitude difference between two observations separated by a rest-frame time lag $\Delta\tau$ ($\Delta\tau = \Delta\tau^{ob}/(1+z)$, $\Delta\tau^{ob}$ is a time lag in the observer frame), and σ_e^2 is the sum of the squared uncertainties for these two magnitudes. To compute the $SF(\Delta\tau)$ for each blazar group, we binned the data using a 200-day (rest frame) step size for $\Delta\tau$ and calculated the average $SF(\Delta\tau)$ for each interval. Errors on $SF(\Delta\tau)$ were determined through error propagation as described in Refs. [46,67]. Figure 8 illustrates the $SF(\Delta\tau)$ for different blazar subclasses. Figure 8 presents the structure function (SF) as a function of time lag ($\Delta\tau$) for various blazar subclasses. A visual inspection of these plots reveals several key trends:

(i) All ESF curves exhibit a consistent profile characterized by an initial rise at shorter time lags followed by a plateau or gradual decline at longer time scales, a trend also observed in the studies of long-term quasar variability in the optical band (e.g., [67–69]). This suggests a common variability mechanism across blazar subclasses. Within the approximate $\Delta\tau$ range of 120 to 2000 days, a power-law increase (i.e., $SF \propto \Delta\tau^\beta$, where β is the power-law index) is evident for all blazar subclasses. The best-fit β values for these subclasses range from 0.09 to 0.19, which are lower than the predicted value of 0.5 for the damped random walk (DRW) model, a stochastic model often used to describe the quasar variability [70]. This suggests that additional factors, such as relativistic beaming and intrinsic blazar properties, contribute to the observed β values. A comparison of the best-fit β values reveals that FSRQs exhibited a shallower ESF compared to BL Lacs, Fermi blazars exhibited a shallower ESF compared to BL Lacs, and LSPs exhibited a shallower ESF compared to ISPs and HSPs.

(ii) Within the approximate $\Delta\tau$ range of 120 to 3900 days, FSRQs exhibited higher ESF values than BL Lacs, indicating greater variability. Fermi blazars displayed more pronounced variability than non-Fermi blazars, as evidenced by their higher ESF values. A clear decreasing trend in ESF values was observed from LSPs to ISPs, and then to HSPs, suggesting that LSPs exhibited greater variability than both ISPs and HSPs. These ESF results are consistent with those obtained from long-term σ_m analysis.

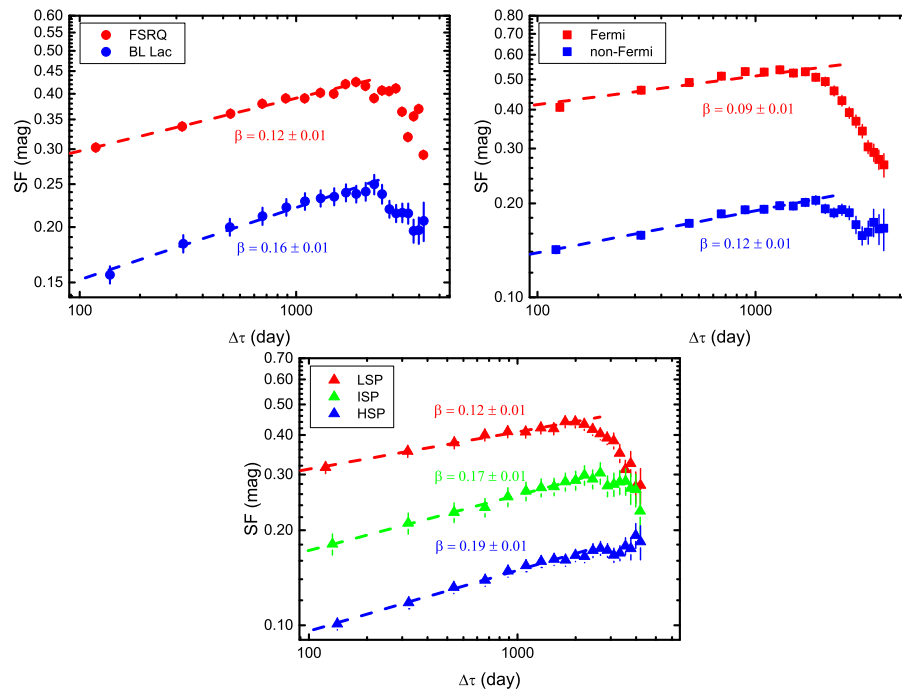


Figure 8. Ensemble structure functions (ESFs) for blazar subclasses. ESFs are shown in the rest frame (log–log scale) for various blazar subclasses. Upper panels: Comparison of ESF between (left) FSRQs and BL Lacs, and (right) Fermi and non-Fermi blazars. (lower): Comparison of ESF among LSP, ISP, and HSP blazars. Dashed lines represent power-law fits to the ESFs ($SF \propto \Delta\tau^\beta$) within the approximate $\Delta\tau$ range of 120 to 2000 days. Best-fit β values are shown near the lines.

4. Summary and Discussion

In this work we constructed a comprehensive dataset of 69,503 short-term 3.4 μ m (W1 band) light curves for 3816 blazars using WISE data spanning up to December 2022. Additionally, we derived a representative long-term 3.4 μ m light curve for each source through epoch averaging. A comparative analysis of short- and long-term intrinsic variability amplitude (σ_m), duty cycle (DC), and ensemble structure function (ESF) across blazar subclasses revealed significant differences in 3.4 μ m flux variability. Our findings are summarized as follows:

- FSRQs exhibited larger σ_m and DC values compared to BL Lacs.
- LSPs displayed larger σ_m and DC values relative to ISPs and HSPs.
- Fermi blazars demonstrated higher long-term σ_m but lower short-term σ_m relative to non-Fermi blazars, with similar DC distributions between the two groups.
- ESF analysis further confirmed the greater variability of FSRQs, LSPs, and Fermi blazars across a wide range of time scales compared to BL Lacs, ISPs/HSPs, and non-Fermi blazars.

Our study represents the most comprehensive statistical analysis of MIR variability among blazars to date. The observed significant disparity in MIR variability across blazar subclasses can be attributed to three primary factors: synchrotron peak frequency, jet power, and Doppler factor.

Within the standard leptonic emission model, W1 band emission is attributed to synchrotron radiation produced by a relativistic electron population with a broken power-law energy distribution [19]. The W1 band covers the declining portion of the synchrotron spectrum for LSPs, while it falls within the rising spectral region for HSPs and ISPs. Lower-energy electrons contribute to the rising synchrotron spectrum, whereas higher-energy particles produce the spectral decline. Given the inverse relationship between cooling time and electron energy ($t_{cool} \propto \gamma^{-1}$, where γ is the Lorentz factor of the electrons), high-energy electrons exhibit faster variability. Consequently, LSPs are anticipated to be more variable

than HSPs and ISPs [71]. As the majority of FSRQs are classified as LSP sources and BL Lac objects as HSP sources, FSRQs are expected to be more variable compared to BL Lacs. Our findings are consistent with the leptonic emission scenario for blazar jets.

Disparities in jet power among blazar subclasses can also contribute to variability differences [46]. For instance, Ref. [72] found larger amplitude optical variability in FSRQs compared to BL Lacs, suggesting higher jet power in FSRQs as a potential cause for more substantial flares. Ref. [31] also found LSPs to be significantly more variable in the optical band than HSPs. The influence of higher jet power in FSRQs/LSPs can also explain the observed variability differences [73,74].

The relativistic Doppler boosting of the jet towards the observer plays a crucial role in non-thermal emission from blazars [4]. Consequently, Doppler effects can contribute to blazar variability. BL Lacs generally exhibit lower Doppler factors than FSRQs, potentially due to a selection bias favoring the detection of more FSRQs at higher redshifts (e.g., [75,76]). Additionally, non-Fermi blazars tend to have lower Doppler factors compared to Fermi blazars (e.g., [22,26]). These Doppler factor differences can also contribute to the observed variability disparities between blazar subclasses.

Fermi blazars exhibited larger long-term σ_m compared to non-Fermi blazars, while displaying lower short-term σ_m . This suggests distinct variability mechanisms dominating on short and long time scales. We propose that the higher Doppler factor in Fermi blazars relative to non-Fermi blazars primarily accounts for their larger long-term σ_m . An analysis of our Fermi and non-Fermi blazar samples revealed that non-Fermi blazars predominantly consist of LSPs (70.3%), while Fermi blazars have a lower LSP fraction (52.3%). This significant difference in LSP composition between the two groups likely explains the larger short-term σ_m observed in non-Fermi blazars relative to Fermi blazars.

This study extends previous studies of MIR variability in blazars [45,46]. Compared to previous studies with 2573 blazars [45] and 1035 Fermi blazars [46], this study encompasses a substantially larger sample of 3816 blazars. Furthermore, this study utilizes WISE data spanning approximately 13 years, significantly extending the temporal coverage of 4 and 7 years in Refs. [45,46]. In this study, an average of eighteen short-term light curves are collected per source, significantly exceeding the eight light curves per source obtained in the previous research by Ref. [46]. This increased dataset allows for a more comprehensive analysis of both short- and long-term variability across various blazar subclasses. Our findings corroborate previous results, including the higher long-term variability of Fermi blazars compared to non-Fermi blazars [45], and the greater variability of FSRQs compared to BL Lacs on both short and long time scales [46]. Additionally, we confirm previous findings [46] that LSP blazars exhibit higher variability than ISP and HSP blazars. This study presents, for the first time, a comparative analysis of short-term σ_m and DC distributions between Fermi and non-Fermi blazars, addressing a gap in previous investigations. Our results reveal that Fermi blazars exhibit lower short-term σ_m values compared to non-Fermi blazars, contrasting with the trend observed for long-term σ_m [45]. Our analysis indicates comparable DC values for Fermi and non-Fermi blazars. Contrary to the findings of Ref. [46], which identified BL Lacs as having higher DC values than FSRQs, our research observed the opposite trend. These new findings may provide valuable insights into the MIR variability properties of blazars.

Author Contributions: Conceptualization, X.Z. and L.M.; methodology, X.Z., Z.H. and L.M.; software, Z.H. and W.H.; validation, X.Z., Z.H. and L.M.; formal analysis, L.M.; investigation, L.M.; resources, X.Z., W.H. and L.M.; data curation, Z.H. and W.H.; writing—original draft preparation, X.Z.; writing—review and editing, X.Z. and L.M.; visualization, Z.H. and W.H.; supervision, X.Z. and L.M.; project administration, L.M.; funding acquisition, L.M. All authors have read and agreed to the published version of the manuscript.

Funding: This work is supported by the National Natural Science Foundation of China (Grant No. 12063007). L.M. acknowledges the Xingdian Talent Support Program of Yunnan Province.

Data Availability Statement: The original data presented in the study (i.e., complete Table 2) are openly available in the National Astronomical Data Center (NADC) of China, <https://paperdata.china-vo.org/MLS/2024/Universe/Table2.csv>, accessed on 24 July 2024.

Acknowledgments: We are grateful to the anonymous reviewers for their thoughtful comments and constructive suggestions, which significantly improved the quality of our manuscript. This work makes use of data products from the Wide-field Infrared Survey Explorer, which is a joint project of the University of California, Los Angeles, and the Jet Propulsion Laboratory/California Institute of Technology, funded by the National Aeronautics and Space Administration. This work also makes use of data products from NEOWISE, which is a project of the Jet Propulsion Laboratory/California Institute of Technology, funded by the Planetary Science Division of the National Aeronautics and Space Administration.

Conflicts of Interest: The authors declare no conflicts of interest.

Notes

- 1 <https://wise2.ipac.caltech.edu/docs/release/allwise>, accessed on 10 December 2023.
- 2 <https://wise2.ipac.caltech.edu/docs/release/neowise>, accessed on 10 December 2023.
- 3 <https://irsa.ipac.caltech.edu/>, accessed on 21 December 2023.
- 4 https://wise2.ipac.caltech.edu/docs/release/allsky/expsup/sec2_4ci.html, accessed on 21 December 2023.
- 5 <https://openuniverse.asi.it/OU4Blazars/MasterListV2/>, accessed on 8 July 2023.
- 6 The *p*-values from the *stats.anderson_ksamp* function are floored/capped at 0.001/0.25.
- 7 <https://pypi.org/project/scikit-posthocs/>, accessed on 23 August 2024.

References

1. Rees, M.J. Black Hole Models for Active Galactic Nuclei. *Annu. Rev. Astron. Astrophys.* **1984**, *22*, 471–506. [\[CrossRef\]](#)
2. Antonucci, R. Unified models for active galactic nuclei and quasars. *Annu. Rev. Astron. Astrophys.* **1993**, *31*, 473–521. [\[CrossRef\]](#)
3. Urry, C.M.; Padovani, P. Unified Schemes for Radio-Loud Active Galactic Nuclei. *Publ. Astron. Soc. Pac.* **1995**, *107*, 803. [\[CrossRef\]](#)
4. Blandford, R.D.; Königl, A. Relativistic jets as compact radio sources. *Astrophys. J.* **1979**, *232*, 34–48. [\[CrossRef\]](#)
5. Ackermann, M.; Anantua, R.; Asano, K.; Baldini, L.; Barbiellini, G.; Bastieri, D.; Becerra Gonzalez, J.; Bellazzini, R.; Bissaldi, E.; Blandford, R.D.; et al. Minute-timescale >100 MeV γ -Ray Variability during the Giant Outburst of Quasar 3C 279 Observed by Fermi-LAT in 2015 June. *Astrophys. J. Lett.* **2016**, *824*, L20. [\[CrossRef\]](#)
6. Fan, J.H.; Kurtanidze, S.O.; Liu, Y.; Kurtanidze, O.M.; Nikolashvili, M.G.; Liu, X.; Zhang, L.X.; Cai, J.T.; Zhu, J.T.; He, S.L.; et al. Optical Photometry of the Quasar 3C 454.3 during the Period 2006–2018 and the Long-term Periodicity Analysis. *Astrophys. J. Suppl. Ser.* **2021**, *253*, 10. [\[CrossRef\]](#)
7. Angelakis, E.; Hovatta, T.; Blinov, D.; Pavlidou, V.; Kiehlmann, S.; Myserlis, I.; Böttcher, M.; Mao, P.; Panopoulou, G.V.; Liodakis, I.; et al. RoboPol: The optical polarization of gamma-ray-loud and gamma-ray-quiet blazars. *Mon. Not. R. Astron. Soc.* **2016**, *463*, 3365–3380. [\[CrossRef\]](#)
8. Aller, M.F.; Aller, H.D.; Hughes, P.A. Pearson-Readhead Survey Sources: Properties of the Centimeter-Wavelength Flux and Polarization of a Complete Radio Sample. *Astrophys. J.* **1992**, *399*, 16. [\[CrossRef\]](#)
9. Liodakis, I.; Marscher, A.P.; Agudo, I.; Berdyugin, A.V.; Bernardos, M.I.; Bonnoli, G.; Borman, G.A.; Casadio, C.; Casanova, V.; Cavazzuti, E.; et al. Polarized blazar X-rays imply particle acceleration in shocks. *Nature* **2022**, *611*, 677–681. [\[CrossRef\]](#)
10. Massaro, F.; Thompson, D.J.; Ferrara, E.C. The extragalactic gamma-ray sky in the Fermi era. *Astron. Astrophys. Rev.* **2015**, *24*, 2. [\[CrossRef\]](#)
11. Pei, Z.Y.; Fan, J.H.; Bastieri, D.; Yang, J.H.; Xiao, H.B.; Yang, W.X. The relationship between the radio core-dominance parameter and spectral index in different classes of extragalactic radio sources (III). *Res. Astron. Astrophys.* **2020**, *20*, 025. [\[CrossRef\]](#)
12. Stocke, J.T.; Morris, S.L.; Gioia, I.M.; Maccacaro, T.; Schild, R.; Wolter, A.; Fleming, T.A.; Henry, J.P. The Einstein Observatory Extended Medium-Sensitivity Survey. II. The Optical Identifications. *Astrophys. J. Suppl.* **1991**, *76*, 813. [\[CrossRef\]](#)
13. Scarpa, R.; Falomo, R. Are high polarization quasars and BL Lacertae objects really different? A study of the optical spectral properties. *Astron. Astrophys.* **1997**, *325*, 109–123.
14. Donato, D.; Ghisellini, G.; Tagliaferri, G.; Fossati, G. Hard X-ray properties of blazars. *Astron. Astrophys.* **2001**, *375*, 739–751. [\[CrossRef\]](#)
15. Mao, L.S.; Xie, G.Z.; Bai, J.M.; Liu, H.T. Statistical Properties of a Blazar Sample and Comparison of HBLs, LBLs and FSRQs. *Chin. J. Astron. Astrophys.* **2005**, *5*, 471–486. [\[CrossRef\]](#)
16. Ghisellini, G.; Tavecchio, F.; Foschini, L.; Ghirlanda, G. The transition between BL Lac objects and flat spectrum radio quasars. *Mon. Not. R. Astron. Soc.* **2011**, *414*, 2674–2689. [\[CrossRef\]](#)
17. Fossati, G.; Maraschi, L.; Celotti, A.; Comastri, A.; Ghisellini, G. A unifying view of the spectral energy distributions of blazars. *Mon. Not. R. Astron. Soc.* **1998**, *299*, 433–448. [\[CrossRef\]](#)

18. Mao, P.; Urry, C.M.; Massaro, F.; Paggi, A.; Cauteruccio, J.; Künzel, S.R. A Comprehensive Statistical Description of Radio-through-Gamma-Ray Spectral Energy Distributions of All Known Blazars. *Astrophys. J. Suppl. Ser.* **2016**, *224*, 26. [\[CrossRef\]](#)

19. Böttcher, M.; Reimer, A.; Sweeney, K.; Prakash, A. Leptonic and Hadronic Modeling of Fermi-detected Blazars. *Astrophys. J.* **2013**, *768*, 54. [\[CrossRef\]](#)

20. Abdo, A.A.; Ackermann, M.; Agudo, I.; Ajello, M.; Aller, H.D.; Aller, M.F.; Angelakis, E.; Arkharov, A.A.; Axelsson, M.; Bach, U.; et al. The Spectral Energy Distribution of Fermi Bright Blazars. *Astrophys. J.* **2010**, *716*, 30–70. [\[CrossRef\]](#)

21. Ajello, M.; Baldini, L.; Ballet, J.; Bastieri, D.; Becerra Gonzalez, J.; Bellazzini, R.; Berretta, A.; Bissaldi, E.; Bonino, R.; Brill, A.; et al. The Fourth Catalog of Active Galactic Nuclei Detected by the Fermi Large Area Telescope: Data Release 3. *Astrophys. J. Suppl. Ser.* **2022**, *263*, 24. [\[CrossRef\]](#)

22. Wu, Z.; Jiang, D.; Gu, M.; Chen, L. Why are some BL Lacertae detected by Fermi, but others not? *Astron. Astrophys.* **2014**, *562*, A64. [\[CrossRef\]](#)

23. Lister, M.L.; Aller, M.F.; Aller, H.D.; Hovatta, T.; Max-Moerbeck, W.; Readhead, A.C.S.; Richards, J.L.; Ros, E. Why Have Many of the Brightest Radio-loud Blazars Not Been Detected in Gamma-Rays by Fermi? *Astrophys. J. Lett.* **2015**, *810*, L9. [\[CrossRef\]](#)

24. Deng, X.J.; Xue, R.; Wang, Z.R.; Xi, S.Q.; Xiao, H.B.; Du, L.M.; Xie, Z.H. The physical properties of γ -ray-quiet flat-spectrum radio quasars: Why are they undetected by Fermi-LAT? *Mon. Not. R. Astron. Soc.* **2021**, *506*, 5764–5773. [\[CrossRef\]](#)

25. Xiong, D.; Zhang, X.; Bai, J.; Zhang, H. Basic properties of Fermi blazars and the ‘blazar sequence’. *Mon. Not. R. Astron. Soc.* **2015**, *450*, 3568–3578. [\[CrossRef\]](#)

26. Savolainen, T.; Homan, D.C.; Hovatta, T.; Kadler, M.; Kovalev, Y.Y.; Lister, M.L.; Ros, E.; Zensus, J.A. Relativistic beaming and gamma-ray brightness of blazars. *Astron. Astrophys.* **2010**, *512*, A24. [\[CrossRef\]](#)

27. Pushkarev, A.B.; Kovalev, Y.Y.; Lister, M.L.; Savolainen, T. Jet opening angles and gamma-ray brightness of AGN. *Astron. Astrophys.* **2009**, *507*, L33–L36. [\[CrossRef\]](#)

28. Lister, M.L.; Homan, D.C.; Kadler, M.; Kellermann, K.I.; Kovalev, Y.Y.; Ros, E.; Savolainen, T.; Zensus, J.A. A Connection Between Apparent VLBA Jet Speeds and Initial Active Galactic Nucleus Detections Made by the Fermi Gamma-Ray Observatory. *Astrophys. J. Lett.* **2009**, *696*, L22–L26. [\[CrossRef\]](#)

29. Piner, B.G.; Pushkarev, A.B.; Kovalev, Y.Y.; Marvin, C.J.; Arenson, J.G.; Charlot, P.; Fey, A.L.; Collioud, A.; Voitsik, P.A. Relativistic Jets in the Radio Reference Frame Image Database. II. Blazar Jet Accelerations from the First 10 Years of Data (1994–2003). *Astrophys. J.* **2012**, *758*, 84. [\[CrossRef\]](#)

30. Pushkarev, A.B.; Kovalev, Y.Y. Single-epoch VLBI imaging study of bright active galactic nuclei at 2 GHz and 8 GHz. *Astron. Astrophys.* **2012**, *544*, A34. [\[CrossRef\]](#)

31. Hovatta, T.; Pavlidou, V.; King, O.G.; Mahabal, A.; Sesar, B.; Dancikova, R.; Djorgovski, S.G.; Drake, A.; Laher, R.; Levitan, D.; et al. Connection between optical and γ -ray variability in blazars. *Mon. Not. R. Astron. Soc.* **2014**, *439*, 690–702. [\[CrossRef\]](#)

32. Fuhrmann, L.; Angelakis, E.; Zensus, J.A.; Nestoras, I.; Marchili, N.; Pavlidou, V.; Karamanavis, V.; Ungerechts, H.; Krichbaum, T.P.; Larsson, S.; et al. The F-GAMMA programme: Multi-frequency study of active galactic nuclei in the Fermi era. Programme description and the first 2.5 years of monitoring. *Astron. Astrophys.* **2016**, *596*, A45. [\[CrossRef\]](#)

33. Bhatta, G.; Webb, J. Microvariability in BL Lacertae: “Zooming” into the Innermost Blazar Regions. *Galaxies* **2018**, *6*, 2. [\[CrossRef\]](#)

34. Wagner, S.J.; Witzel, A. Intraday Variability In Quasars and BL Lac Objects. *Annu. Rev. Astron. Astrophys.* **1995**, *33*, 163–198. [\[CrossRef\]](#)

35. Gupta, A.C.; Fan, J.H.; Bai, J.M.; Wagner, S.J. Optical Intra-Day Variability in Blazars. *Astron. J.* **2008**, *135*, 1384–1394. [\[CrossRef\]](#)

36. Sandrinelli, A.; Covino, S.; Treves, A. Long and short term variability of seven blazars in six near-infrared/optical bands. *Astron. Astrophys.* **2014**, *562*, A79. [\[CrossRef\]](#)

37. Fan, J.H.; Xie, G.Z.; Pecontal, E.; Pecontal, A.; Copin, Y. Historic Light Curve and Long-Term Optical Variation of BL Lacertae 2200 + 420. *Astrophys. J.* **1998**, *507*, 173–178. [\[CrossRef\]](#)

38. Villforth, C.; Nilsson, K.; Heidt, J.; Takalo, L.O.; Pursimo, T.; Berdyugin, A.; Lindfors, E.; Pasanen, M.; Winiarski, M.; Drozdz, M.; et al. Variability and stability in blazar jets on time-scales of years: Optical polarization monitoring of OJ 287 in 2005–2009. *Mon. Not. R. Astron. Soc.* **2010**, *402*, 2087–2111. [\[CrossRef\]](#)

39. Bonning, E.; Urry, C.M.; Baily, C.; Buxton, M.; Chatterjee, R.; Coppi, P.; Fossati, G.; Isler, J.; Maraschi, L. SMARTS Optical and Infrared Monitoring of 12 Gamma-Ray Bright Blazars. *Astrophys. J.* **2012**, *756*, 13. [\[CrossRef\]](#)

40. Safna, P.Z.; Stalin, C.S.; Rakshit, S.; Mathew, B. Long-term optical and infrared variability characteristics of Fermi blazars. *Mon. Not. R. Astron. Soc.* **2020**, *498*, 3578–3591. [\[CrossRef\]](#)

41. Gupta, A.C.; Kushwaha, P.; Carrasco, L.; Xu, H.; Wiita, P.J.; Escobedo, G.; Porras, A.; Recillas, E.; Mayya, Y.D.; Chavushyan, V.; et al. Long-term Multiband Near-infrared Variability of the Blazar OJ 287 during 2007–2021. *Astrophys. J. Suppl. Ser.* **2022**, *260*, 39. [\[CrossRef\]](#)

42. Wright, E.L.; Eisenhardt, P.R.M.; Mainzer, A.K.; Ressler, M.E.; Cutri, R.M.; Jarrett, T.; Kirkpatrick, J.D.; Padgett, D.; McMillan, R.S.; Skrutskie, M.; et al. The Wide-field Infrared Survey Explorer (WISE): Mission Description and Initial On-orbit Performance. *Astron. J.* **2010**, *140*, 1868–1881. [\[CrossRef\]](#)

43. Mainzer, A.; Bauer, J.; Grav, T.; Masiero, J.; Cutri, R.M.; Dailey, J.; Eisenhardt, P.; McMillan, R.S.; Wright, E.; Walker, R.; et al. Preliminary Results from NEOWISE: An Enhancement to the Wide-field Infrared Survey Explorer for Solar System Science. *Astrophys. J.* **2011**, *731*, 53. [\[CrossRef\]](#)

44. Mainzer, A.; Bauer, J.; Cutri, R.M.; Grav, T.; Masiero, J.; Beck, R.; Clarkson, P.; Conrow, T.; Dailey, J.; Eisenhardt, P.; et al. Initial Performance of the NEOWISE Reactivation Mission. *Astrophys. J.* **2014**, *792*, 30. [\[CrossRef\]](#)

45. Mao, L.; Zhang, X.; Yi, T. Mid-infrared variability of blazars: A view from NEOWISE survey. *Astrophys. Space Sci.* **2018**, *363*, 167. [\[CrossRef\]](#)

46. Anjum, A.; Stalin, C.S.; Rakshit, S.; Gudennavar, S.B.; Durgapal, A. Mid-infrared variability of γ -ray emitting blazars. *Mon. Not. R. Astron. Soc.* **2020**, *494*, 764–774. [\[CrossRef\]](#)

47. Massaro, E.; Giommi, P.; Leto, C.; Marchegiani, P.; Maselli, A.; Perri, M.; Piranomonte, S.; Sclavi, S. Roma-BZCAT: A multifrequency catalogue of blazars. *Astron. Astrophys.* **2009**, *495*, 691–696. [\[CrossRef\]](#)

48. Ackermann, M.; Ajello, M.; Atwood, W.B.; Baldini, L.; Ballet, J.; Barbiellini, G.; Bastieri, D.; Becerra Gonzalez, J.; Bellazzini, R.; Bissaldi, E.; et al. The Third Catalog of Active Galactic Nuclei Detected by the Fermi Large Area Telescope. *Astrophys. J.* **2015**, *810*, 14. [\[CrossRef\]](#)

49. Ajello, M.; Angioni, R.; Axelsson, M.; Ballet, J.; Barbiellini, G.; Bastieri, D.; Becerra Gonzalez, J.; Bellazzini, R.; Bissaldi, E.; Bloom, E.D.; et al. The Fourth Catalog of Active Galactic Nuclei Detected by the Fermi Large Area Telescope. *Astrophys. J.* **2020**, *892*, 105. [\[CrossRef\]](#)

50. Rakshit, S.; Johnson, A.; Stalin, C.S.; Gandhi, P.; Hoenig, S. WISE view of narrow-line Seyfert 1 galaxies: Mid-infrared colour and variability. *Mon. Not. R. Astron. Soc.* **2019**, *483*, 2362–2370. [\[CrossRef\]](#)

51. Kudryavtsev, D.O.; Sotnikova, Y.V.; Stolyarov, V.A.; Mufakharov, T.V.; Vlasyuk, V.V.; Khabibullina, M.L.; Mikhailov, A.G.; Cherepkova, Y.V. Cluster Analysis of the Roma-BZCAT Blazars. *Res. Astron. Astrophys.* **2024**, *24*, 055011. [\[CrossRef\]](#)

52. Giommi, P.; Brandt, C.H.; Barres de Almeida, U.; Pollock, A.M.T.; Arneodo, F.; Chang, Y.L.; Civitarese, O.; De Angelis, M.; D'Elia, V.; Del Rio Vera, J.; et al. Open Universe for Blazars: A new generation of astronomical products based on 14 years of Swift-XRT data. *Astron. Astrophys.* **2019**, *631*, A116. [\[CrossRef\]](#)

53. Sesar, B.; Ivezić, Ž.; Lupton, R.H.; Jurić, M.; Gunn, J.E.; Knapp, G.R.; DeLee, N.; Smith, J.A.; Miknaitis, G.; Lin, H.; et al. Exploring the Variable Sky with the Sloan Digital Sky Survey. *Astron. J.* **2007**, *134*, 2236–2251. [\[CrossRef\]](#)

54. Ai, Y.L.; Yuan, W.; Zhou, H.Y.; Wang, T.G.; Dong, X.B.; Wang, J.G.; Lu, H.L. Dependence of the Optical/Ultraviolet Variability on the Emission-line Properties and Eddington Ratio in Active Galactic Nuclei. *Astrophys. J. Lett.* **2010**, *716*, L31–L35. [\[CrossRef\]](#)

55. Jarrett, T.H.; Cohen, M.; Masci, F.; Wright, E.; Stern, D.; Benford, D.; Blain, A.; Carey, S.; Cutri, R.M.; Eisenhardt, P.; et al. The Spitzer-WISE Survey of the Ecliptic Poles. *Astrophys. J.* **2011**, *735*, 112. [\[CrossRef\]](#)

56. Kundu, A.; Chatterjee, R.; Mitra, K.; Mondal, S. rms-flux relation and disc-jet connection in blazars in the context of the internal shocks model. *Mon. Not. R. Astron. Soc.* **2022**, *510*, 3688–3700. [\[CrossRef\]](#)

57. Giebels, B.; Degrange, B. Lognormal variability in BL Lacertae. *Astron. Astrophys.* **2009**, *503*, 797–799. [\[CrossRef\]](#)

58. Kushwaha, P.; Sinha, A.; Misra, R.; Singh, K.P.; de Gouveia Dal Pino, E.M. Gamma-Ray Flux Distribution and Nonlinear Behavior of Four LAT Bright AGNs. *Astrophys. J.* **2017**, *849*, 138. [\[CrossRef\]](#)

59. Bhatta, G. Characterizing Long-term Optical Variability Properties of γ -Ray-bright Blazars. *Astrophys. J.* **2021**, *923*, 7. [\[CrossRef\]](#)

60. Scholz, F.W.; Stephens, M.A. K-sample Anderson–Darling tests. *J. Am. Stat. Assoc.* **1987**, *82*, 918–924.

61. Virtanen, P.; Gommers, R.; Oliphant, T.E.; Haberland, M.; Reddy, T.; Cournapeau, D.; Burovski, E.; Peterson, P.; Weckesser, W.; Bright, J.; et al. SciPy 1.0: Fundamental algorithms for scientific computing in Python. *Nat. Methods* **2020**, *17*, 261–272. [\[CrossRef\]](#)

62. Kruskal, W.H.; Wallis, W.A. Use of ranks in one-criterion variance analysis. *J. Am. Stat. Assoc.* **1952**, *47*, 583–621. [\[CrossRef\]](#)

63. Dunn, O.J. Multiple comparisons using rank sums. *Technometrics* **1964**, *6*, 241–252. [\[CrossRef\]](#)

64. Romero, G.E.; Cellone, S.A.; Combi, J.A. Optical microvariability of southern AGNs. *Astron. Astrophys. Suppl.* **1999**, *135*, 477–486. [\[CrossRef\]](#)

65. Bevington, P.R. *Data Reduction and Error Analysis for the Physical Sciences*; McGraw-Hill Education: New York, NY, USA, 1969.

66. Emmanoulopoulos, D.; McHardy, I.M.; Uttley, P. On the use of structure functions to study blazar variability: Caveats and problems. *Mon. Not. R. Astron. Soc.* **2010**, *404*, 931–946. [\[CrossRef\]](#)

67. Vanden Berk, D.E.; Wilhite, B.C.; Kron, R.G.; Anderson, S.F.; Brunner, R.J.; Hall, P.B.; Ivezić, Ž.; Richards, G.T.; Schneider, D.P.; York, D.G.; et al. The Ensemble Photometric Variability of $\sim 25,000$ Quasars in the Sloan Digital Sky Survey. *Astrophys. J.* **2004**, *601*, 692–714. [\[CrossRef\]](#)

68. Gallastegui-Aizpun, U.; Sarajedini, V.L. The ensemble optical variability of type-1 AGN in the Sloan Digital Sky Survey Data Release 7. *Mon. Not. R. Astron. Soc.* **2014**, *444*, 3078–3088. [\[CrossRef\]](#)

69. Kozłowski, S. Revisiting Stochastic Variability of AGNs with Structure Functions. *Astrophys. J.* **2016**, *826*, 118. [\[CrossRef\]](#)

70. Kelly, B.C.; Bechtold, J.; Siemiginowska, A. Are the Variations in Quasar Optical Flux Driven by Thermal Fluctuations? *Astrophys. J.* **2009**, *698*, 895–910. [\[CrossRef\]](#)

71. Paliya, V.S.; Stalin, C.S.; Ajello, M.; Kaur, A. Intra-night Optical Variability Monitoring of Fermi Blazars: First Results from 1.3 m J. C. Bhattacharya Telescope. *Astrophys. J.* **2017**, *844*, 32. [\[CrossRef\]](#)

72. Bauer, A.; Baltay, C.; Coppi, P.; Ellman, N.; Jerke, J.; Rabinowitz, D.; Scalzo, R. Blazar Optical Variability in the Palomar-Quest Survey. *Astrophys. J.* **2009**, *699*, 1732–1741. [\[CrossRef\]](#)

73. Gardner, E.; Done, C. What powers the most relativistic jets?–I. BL Lacs. *Mon. Not. R. Astron. Soc.* **2014**, *438*, 779–788. [\[CrossRef\]](#)

74. Gardner, E.; Done, C. What powers the most relativistic jets?–II. Flat-spectrum radio quasars. *Mon. Not. R. Astron. Soc.* **2018**, *473*, 2639–2654. [\[CrossRef\]](#)

75. Lister, M.L.; Aller, M.F.; Aller, H.D.; Homan, D.C.; Kellermann, K.I.; Kovalev, Y.Y.; Pushkarev, A.B.; Richards, J.L.; Ros, E.; Savolainen, T. MOJAVE. X. Parsec-scale Jet Orientation Variations and Superluminal Motion in Active Galactic Nuclei. *Astron. J.* **2013**, *146*, 120. [[CrossRef](#)]
76. Liodakis, I.; Pavlidou, V. Population statistics of beamed sources-I. A new model for blazars. *Mon. Not. R. Astron. Soc.* **2015**, *451*, 2434–2446. [[CrossRef](#)]

Disclaimer/Publisher’s Note: The statements, opinions and data contained in all publications are solely those of the individual author(s) and contributor(s) and not of MDPI and/or the editor(s). MDPI and/or the editor(s) disclaim responsibility for any injury to people or property resulting from any ideas, methods, instructions or products referred to in the content.